Article

Enhanced Photocatalytic Degradation of Organic Dyes via Defect-Rich TiO$_2$ Prepared by Dielectric Barrier Discharge Plasma

Yanqin Li [1], Wei Wang [1], Fu Wang [2] , Lanbo Di [3] , Shengchao Yang [1], Shengjie Zhu [1], Yongbin Yao [1], Cunhua Ma [1], Bin Dai [1] and Feng Yu [1,*]

[1] Key Laboratory for Green Processing of Chemical Engineering of Xinjiang Bingtuan, School of Chemistry and Chemical Engineering, Shihezi University, Shihezi 832003, China; liyanqin112@163.com (Y.L.); wangw@shzu.edu.cn (W.W.); shengchao.yang@shzu.edu.cn (S.Y.); zsj97262724@163.com (S.Z.); yongbinyao0321@sina.com (Y.Y.); mchua@shzu.edu.cn (C.M.); db_tea@shzu.edu.cn (B.D.)

[2] School of Environmental Science and Engineering, Shanghai Jiao Tong University, Shanghai 200240, China; wangfu@sjtu.edu.cn

[3] College of Physical Science and Technology, Dalian University, Dalian 116622, China; dilanbo@163.com

* Correspondence: yufeng05@mails.ucas.ac.cn or yufeng05@mail.ipc.ac.cn

Abstract: The dye wastewater produced in the printing and dyeing industry causes serious harm to the natural environment. TiO$_2$ usually shows photocatalytic degradation of dye under the irradiation ultravilet light rather than visible light. In this work, a large number of oxygen vacancies and Ti^{3+} defects were generated on the surface of the TiO$_2$ nanoparticles via Ar plasma. Compared with pristine TiO$_2$ nanoparticles, the as-obtained Ar plasma-treated TiO$_2$ (Ar-TiO$_2$) nanoparticles make the energy band gap reduce from 3.21 eV to 3.17 eV and exhibit enhanced photocatalytic degradation of organic dyes. The Ar-TiO$_2$ obtained exhibited excellent degradation properties of methyl orange (MO); the degradation rate under sunlight irradiation was 99.6% in 30 min, and the photocatalytic performance was about twice that of the original TiO$_2$ nanoparticles (49%). The degradation rate under visible light ($\lambda > 400$ nm) irradiation was 89% in 150 min, and the photocatalytic performance of the Ar-TiO$_2$ was approaching ~4 times higher than that of the original TiO$_2$ nanoparticles (23%). Ar-TiO$_2$ also showed good degradation performance in degrading rhodamine B (Rho B) and methylene blue (MB). We believe that this plasma strategy provides a new method for improving the photocatalytic activity of other metal oxides.

Keywords: titanium dioxide; plasma; photocatalytic degradation; organic dye; defects

1. Introduction

Printing and dyeing wastewater has caused serious pollution to the environment [1,2], and it is necessary to seek an effective treatment of printing and dyeing wastewater [3]. Semiconductor photocatalytic technology has attracted much attention due to its excellent application prospects in the fields of sewage treatment, air purification, cleaning and sterilization, and solar energy conversion [4–6]. It is also an advanced technology that uses solar energy to carry out chemical reactions in a mild environment [7–9]. Compared with the traditional pollutant treatment methods, it has the characteristics of mild reaction conditions, complete mineralization of pollutants, high efficiency and high stability, and no secondary pollution. Therefore, it is particularly important to construct an efficient photocatalyst with visible light response and to conduct an in-depth study of its mechanism.

Recently, photocatalysts have been catalytically active substances that can be used in the environment, including water or air purification, water splitting to produce hydrogen, carbon

dioxide catalytic reduction and antibacterial action [10–15]. Among semiconductor materials, titanium dioxide (TiO_2) is widely used as a photocatalyst due to its good oxidation and hydrophilic properties, excellent chemical durability and low cost [16–19]. However, TiO_2 can only be activated by ultraviolet (UV) light ($\lambda < 380$ nm) due to its wide band gap (3.0–3.2 eV). UV light contains about 5% of solar energy reaching the land surface [20,21], and it is crucial to increase the photoabsorption range of TiO_2 to improve solar energy utilization. TiO_2 materials can achieve excellent optical absorption properties by doping [22–27].

To improve the photocatalytic performance of TiO_2, some transition metal oxides were introduced into TiO_2, such as FeO_x [28], CuO_x [29,30], NiO [31], CeO_2 [32] and ZnO [33]. Metal doping could make electrons easier to excite and reduce the recombination of electron-hole pairs of TiO_2 [34–36]. Furthermore, enhanced photo-response could be obtained by TiO_2 with doping non-metals, such as N [37], C [38], F [39] and S [40]. In addition, the defects generated on the surface of TiO_2 are able to effectively hinder the recombination of photogenerated electron-hole pairs. Surface defects of TiO_2, for instance, Ti^{3+} defects and oxygen vacancies, promote the formation of the original intermediate band, which plays an important role in photoelectron capture [41].

Low temperature plasma can cause defects and oxygen vacancies on the catalyst surface to improve the catalytic efficiency [42–44]. The effect of treating the catalyst with low temperature plasma under different atmospheres is different. Nanowires and nanoparticles of TiO_2 treated under a hot hydrogen atmosphere have better photocatalytic degradation of dye properties because of the presence of oxygen vacancies and Ti^{3+} forming an intermediate layer [45,46]. The application of oxygen and nitrogen plasma reduced the TiO_2 powder and produced an intermediate state, resulting in an increase in its optical activity in the visible region [47]. The trapping of charge carriers, decreases the electron-hole recombination rate. However catalyst mechanisms, irradiation conditions and defects have not been fully explained.

Herein, we successfully prepared TiO_2 nanoparticles by titanium alkoxide hydrolysis method, and etched them in Ar atmosphere with low temperature dielectric barrier discharge (DBD) plasma [48,49]. The results showed that the plasma-etched TiO_2 nanoparticles had more oxygen vacancies and Ti^{3+} defects than of the original TiO_2, and thus have excellent photocatalytic degradation properties under sunlight. We believe that DBD plasma provides a new strategy for etching the surface of catalysts.

2. Experimental Section

2.1. Sample Preparation

The TiO_2 photocatalyst was prepared using an alkoxide hydrolysis process with titanium n-butoxide (Ti $(OC_4H_9)_4$, *AR*, Macklin, Shanghai, China) used as the precursor for TiO_2. 3 g of titanium n-butoxide was added to 100 g of ethanol (C_2H_5OH, AR, Fuyu Fine Chemical Co., Ltd., Tianjin, China) to obtain a mixed solution A; 5 g of deionized water was dissolved in 100 mL of absolute ethanol and stirred for 30 min to make it evenly mixed to obtain a homogeneous solution B; then the solution A was slowly dropped into solution B, and a white precipitate after about 5 min. The solution obtained was stirred vigorously for 1 h, aged for 12 h, and then the white precipitate was filtered, washed 4 times with the alcohol-water mixture, dried in a drying oven at 80 °C for 24 h, and then ground to obtain TiO_2 nanoparticles. The dried powders were then calcined in air for 5 h with the temperature ranging from 30 to 450 °C. The pristine TiO_2 obtained was separately subjected to plasma treatment in a dielectric barrier discharge (DBD) plasma reactor at a voltage of 50 V, a current of 1.5 A, and an Ar atmosphere for 20 min to obtain TiO_2 (Ar-TiO_2).

2.2. Catalyst Characterization

The catalyst crystal structure was identified by X-ray diffractometer (XRD) with Cu-Kα (40 kV, 40 mA, k = 1.5406 Å and 2θ range from 10–90°) radiation (Karlsruhe, Baden-Württemberg, German). The Raman spectrum was measured by Raman spectroscopy using a Renishaw inVia (Renishaw,

London, UK) with a laser power of 5 mW and a laser excitation of 532 nm (wavenumber range 100–3200 cm^{-1}). Using KBr as diluents, the Fourier transforms infrared spectra (FTIR) of the samples were collected with a Thermo spectrum system (Thermo Fisher Scientific, Massachusetts, MA, USA). The samples were subjected to X-ray photoelectron spectroscopy (XPS, Thermo Scientific Escalab 250Xi, Thermo Fisher Scientific, Massachusetts, MA, USA) by using Al Kα radiation (1486.6 eV). All binding energies were calibrated using the C1s peak (BE = 284.8 eV) as a standard. Morphology and microstructure were determined by transmission electron microscopy (TEM, Tecnai G2 F30 S-TWIN 200 KV, Hillsboro, OR, USA), high resolution TEM (HRTEM) and selective area electron diffraction (SAED). Measurement of electron paramagnetic resonance (EPR) spectra was performed at 300 K using a Bruker A200 EPR spectrometer (Bruker, Karlsruhe, Germany). The samples were subjected to UV-Vis testing using Shimadzu UV3600 (Shimadzu, Tokyo, Japan). Brunauer–Emmett–Teller (BET) surface area, pore volumes and pore diameter of the samples were determined by using a Micromeritics ASAP 2020C surface area and porosity analyzer (Micromeritics ASAP 2020 BET apparatus, Atlanta, Georgia, GA, USA). The samples were degassed for 4 h at 200 degrees and then analyzed using N_2 adsorption-desorption in liquid nitrogen.

2.3. Photocatalytic Activity Measurements

Photocatalytic performance was investigated by using a 300 W Xeon lamp equipped with a 400 nm cut-off filter to degrade methyl orange (MO), rhodamine B (Rho B) and MB under sunlight and visible light. Water cooled the reactor, to keep the temperature at 25 °C. To put it simply, 50 mg photocatalyst was mixed with 100 mL 10 mg·L^{-1} organic dye solution, and the mixed solution was placed 20 cm away from the photosource. Meanwhile, the mixture was stirred stably. The sample solution was then collected every 30 min of irradiation. The solution collected was centrifuged at 10,000 rpm for 2 min, the mixed solution was separated, and the supernatant was extracted for ultraviolet testing. The dye solutions collected (MO, Rho B and MB) were subjected to absorbance detection using UV-Vis (TU-1900). The degradation efficiencies of MO, Rho B and MB were analyzed by changes in absorption peaks at 462, 554 and 660 nm. The degradation rates of MO, Rho B and MB are calculated by the formula $\ln (C_0/C) = kt$, where k is the reaction rate constant, C_0 and C are the initial concentration of the dye and the concentration after the reaction time t.

2.4. Apparent Quantum Efficiency Measurement

The photocatalytic H_2-production experiments were performed in a 300 mL sealed jacket beaker at ambient temperature and atmospheric pressure. In a typical photocatalytic experiment, 100 mg of Ar-TiO_2 composite photocatalyst was suspended in 100 mL of aqueous solution containing methanol (20.0 V%) as sacrificial agents for trapping holes. Proper amount of H_2PtCl_6 aqueous solution was added in the above solution. Therefore, 3.0 wt% Pt, as a co-catalyst, was in-suit reduced during the photocatalytic hydrogen evolution reaction. Then, evacuation was performed with a vacuum pump to ensure that the reactor was under vacuum. A continuous magnetic stirrer was applied at the bottom of the reactor in order to keep the photocatalyst particles in suspension status during the whole experiment. After 0.5 h of irradiation, the chromatographic inlet was opened, and hydrogen was analyzed by gas chromatograph (GC7806, Beijing Shiwei Spectrum Analysis Instrument Co., Ltd., Beijing, China, TCD, with nitrogen as a carrier gas and 5 A molecular sieve column). All glassware was carefully rinsed with deionized water prior to use. The apparent quantum efficiency (AQE) was measured under the same photocatalytic reaction conditions. A Xe lamp source (300 W, 385 nm) was placed 10 cm directly above the reactor to serve as a light source to initiate a photocatalytic reaction. The optical power density of the Xe lamp source is measured by a strong optical power meter (CEL-NP2000)

and the focused area on the beaker is 30 cm^2. We measured and calculated the number of photons according to Equation (1):

$$number_{photons} = \frac{Focused\ intensity \times Focused\ area}{hv} = \frac{Focused\ intensity \times Focused\ area}{h\frac{c}{\lambda}} \tag{1}$$

We measured and calculated apparent quantum efficiencies (AQE) according to Equation (2): [50]

$$AQE(\%) = \frac{number\ of\ reacted\ electrons}{number\ of\ incident\ photons} \times 100 = \frac{number\ of\ evolve\ H_2\ molecules \times 2}{number\ of\ incident\ photons} \times 100 \tag{2}$$

where *h* is the Planck constant (J·s), *c* is Speed of light (m/s) and λ is the wavelength of linght (nm).

3. Results and Discussion

3.1. Physicochemical Properties of Catalysts

Figure 1a shows the XRD pattern of the original TiO$_2$ and Ar-TiO$_2$. It can be seen from the XRD pattern that only the diffraction peak of anatase has no other impurity peaks detected, indicating that the sample contains only anatase. Two samples showed similar peak positions, which were attributed to TiO$_2$ (anatase, PDF#21-1272). The diffraction peaks: 2θ = 25°, 37.5°, 48.4°, 53.5°, 55.3° and 62.2° were assigned to the (101), (004), (200), (211) and (204) lattice planes. The XRD pattern of the modified TiO$_2$ has a higher strength than the original TiO$_2$, which indicated that the Ar plasma caused an improvement in the crystallinity of the modified TiO$_2$. The broadened diffraction peaks indicated that the size of the nanocrystals is small [51]. There was no significant difference between the two samples.
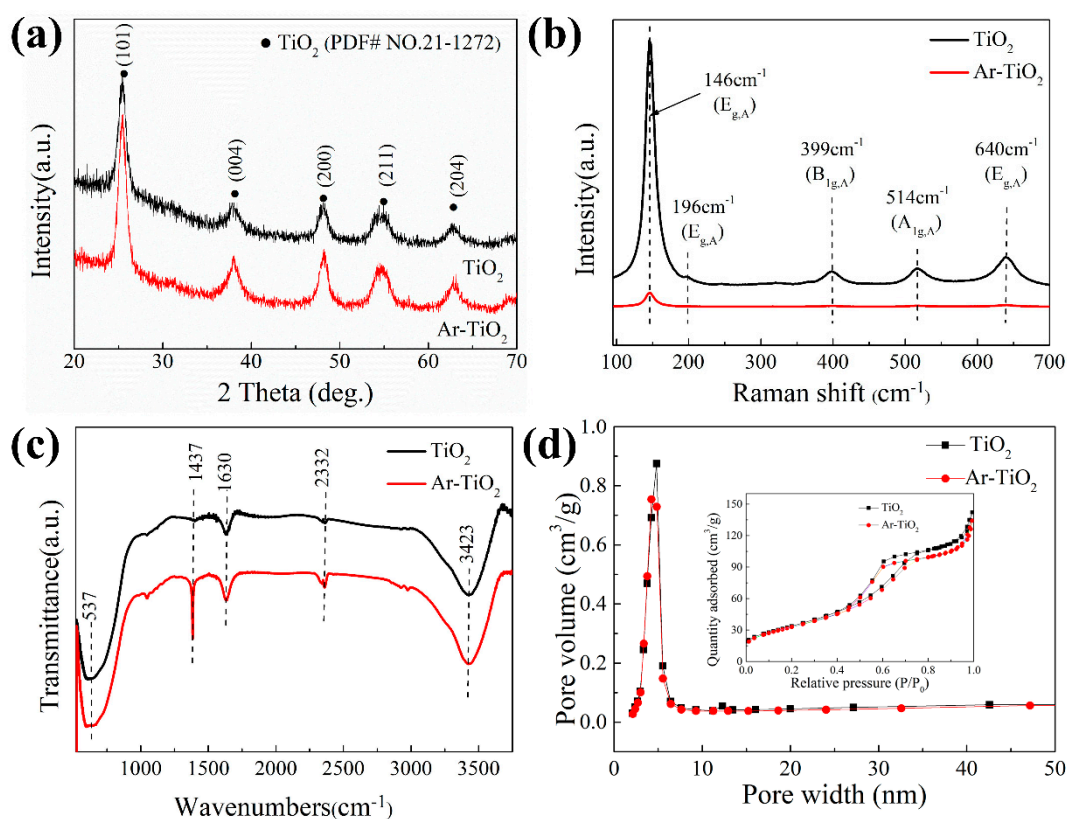

Figure 1. Spectra of (**a**) X-ray diffractometer (XRD) spectra, (**b**) Raman spectra, (**c**) Fourier transforms infrared spectra (FTIR) spectra and (**d**) BET spectra for the Ar-TiO$_2$ and pristine TiO$_2$ catalysts. Insert: the N$_2$ adsorption-desorption isotherms.

Figure 1b shows the Raman spectrum of the original TiO_2 and Ar-TiO_2 in Ar atmosphere. The original sample peaks were: 146 cm^{-1} (E_g), 196 cm^{-1} (E_g), 399 cm^{-1} (B_{1g}), 514 cm^{-1} (A_{1g} or B_{1g}) and 640 cm^{-1} (A_{1g}) respectively typical Anatase phase [52–54]. The treated sample showed a scattering peak only at 146 cm^{-1} (E_g). The peak intensity and width of TiO_2 treated with plasma in Ar atmosphere were lower and wider than those of the original TiO_2. This indicated that there were some defects on the surface of TiO_2 after plasma treatment [55]. The Raman scattering selection rule was broken, indicating the surface characteristics of the disordered phase [56]. Raman analysis showed that the molecular vibration of the surface crystallinity of TiO_2 was seriously affected by the plasma treatment.

The FTIR spectra of the original and Ar-TiO_2 are shown in Figure 1c. An absorption peak appearing near 523 cm^{-1} was due to the Ti-O-Ti bond of nano-titanium dioxide, and the absorption peaks at 3500–3000 cm^{-1} and 1630 cm^{-1} were caused by the tensile vibration of the hydroxyl group. The hydroxyl group was adsorbed on the surface of the material [57]. The C-O band (1437 cm^{-1}) was detected due to the formation of CO_2 on the surface of TiO_2 [58,59].

X-ray photoelectron spectroscopy (XPS) demonstrates the defects and the chemical composition of Ar-TiO_2. The XPS spectra of the elements O 1s and Ti 2p are shown in Figure 2b,c. In Figure 2b, O 1s was divided into three peaks, 530.0, 531.6 and 533.1 eV, respectively, which corresponds with lattice oxygen (O_{latt}), defect oxygen (O_{def}) and surface oxygen (O_{surf}) [60,61].
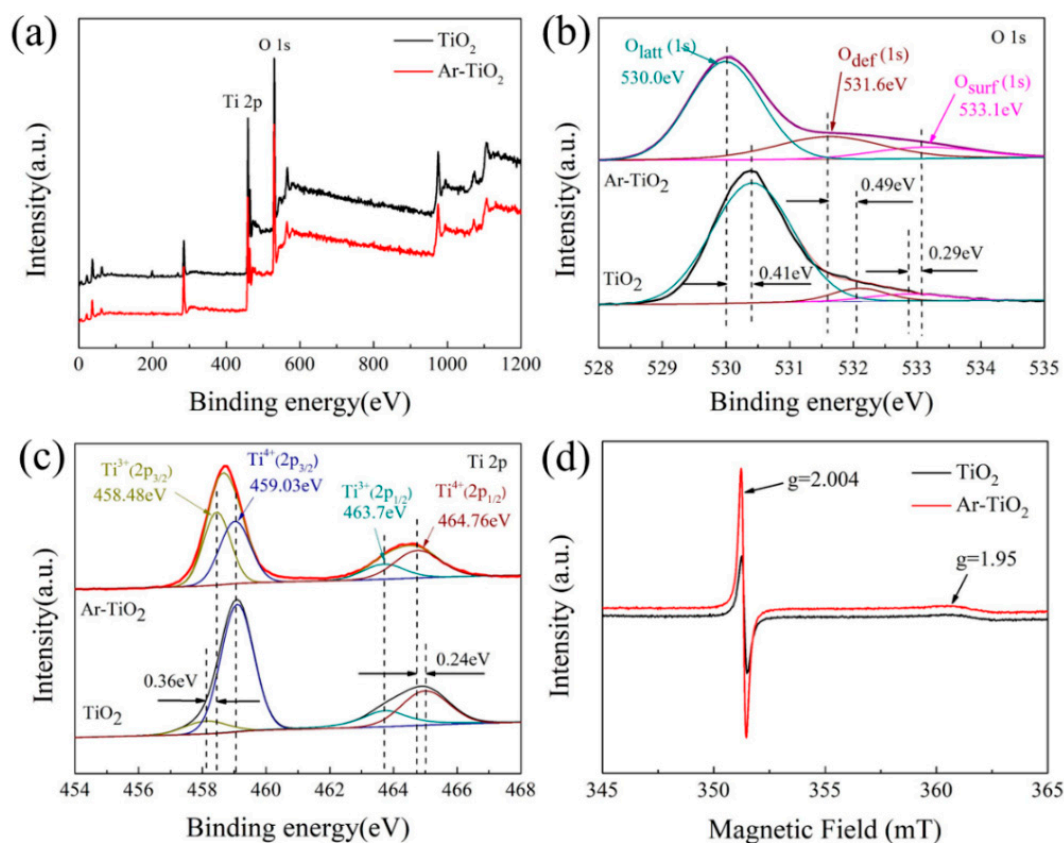
Figure 2. X-ray photoelectron spectroscopy (XPS) spectra of (**a**) survey spectra, (**b**) O 1s, (**c**) Ti 2p and (**d**) Electron paramagnetic resonance (EPR) spectra for the Ar-TiO_2 and pristine TiO_2 catalysts.

Figure 2b shows that, compared with the original TiO_2, the O_{def} content in the Ar-TiO_2 is significantly increased, indicating that the plasma effectively removed oxygen, and thus some oxygen vacancies are produced in the crystal lattice of TiO_2. In calculation, the defect-oxygen content of the plasma-treated TiO_2 was four times that of the original TiO_2 (Table 1) [60].

Table 1. Surface atomic species on the surface of TiO_2 and $Ar-TiO_2$ catalysts.

| Samples	Surface Atomic Concentration (%)	
	Ti^{3+}/Ti	$O_{def}/(O_{latt} + O_{def} + O_{surf})$
TiO_2	20.9	6.0
$Ar-TiO_2$	45.2	24.4

Figure 2c presents the Ti 2p photoelectron spectra of TiO_2, the Ti 2p peaks at 464.76, 463.7, 459.03, and 458.48 eV were observed corresponding to Ti^{4+} $2p_{1/2}$, Ti^{3+} $2p_{1/2}$, Ti^{4+} $2p_{3/2}$, and Ti^{3+} $2p_{3/2}$, respectively [55,62]. However, it can be seen that after the plasma treatment in the Ar atmosphere, the peaks of Ti^{4+} at 459.03 eV and 464.76 eV were shifted by 0.36 eV and 0.24 eV, and the content of Ti^{3+} peak was increased, implying that Ti^{3+} was generated as a result of the Ti^{4+} reduction. A large amount of Ti^{3+} and oxygen vacancy in $Ar-TiO_2$ could make the coordination number of Ti-O-Ti and the surface lattice structure change, thus generating the defects [63]. According to the results of XPS analysis, the plasma-treated titanium dioxide had abundant defects and oxygen vacancies, which played a key role in the degradation of the photocatalyst.

Electron paramagnetic resonance (EPR) was used to further demonstrated oxygen vacancies and Ti^{3+} defects of the samples. The magnetization results recorded at 300 K clearly showed surface oxygen vacancies and unpaired spins electrons of Ti^{3+} 3d1 in the samples. Figure 2d shows the EPR results of the original TiO_2 and $Ar-TiO_2$. The index values of the g peaks at 1.95 and 2.004 corresponded to Ti^{3+} and oxygen vacancies in the TiO_2 lattice, respectively [60,64,65]. The content of Ti^{3+} and oxygen vacancies in plasma treatment were significantly higher than that of the original TiO_2, which was consistent with the analysis results of the XPS spectrum.

In order to test the optical performance of the photocatalyst, UV-Vis among 200 nm and 800 nm was surveyed. As shown in Figure 3a, all of the TiO_2 photocatalysts showed the significant absorption of light in the ultraviolet region (<400 nm) and the light absorption of the $Ar-TiO_2$ photocatalyst moved toward the visible region. The band gap of each sample was estimated by the simulation calculation, TiO_2 was 3.21 eV and the $Ar-TiO_2$ was 3.17 eV (inset of Figure 3a). This value is the effect of the extrapolation to zero $(\alpha h v)^{1/2}$ curve on photon energy, where α is the absorption factor and hv is the light quantum energy [53,56]. Based on the XPS valence band (VB) spectrum (Figure 3b), the valence band position of $Ar-TiO_2$ was 2.93 eV, which was lower than the original TiO_2 (3.02 eV). These results indicated that the oxygen vacancies (or Ti^{3+} species) were produced during the Ar gas plasma treatment and caused the band gap of the $Ar-TiO_2$ photocatalyst to be narrowed. The electronic band-gap structure and photocatalytic degradation mechanism of TiO_2 samples were shown in Figure 4.
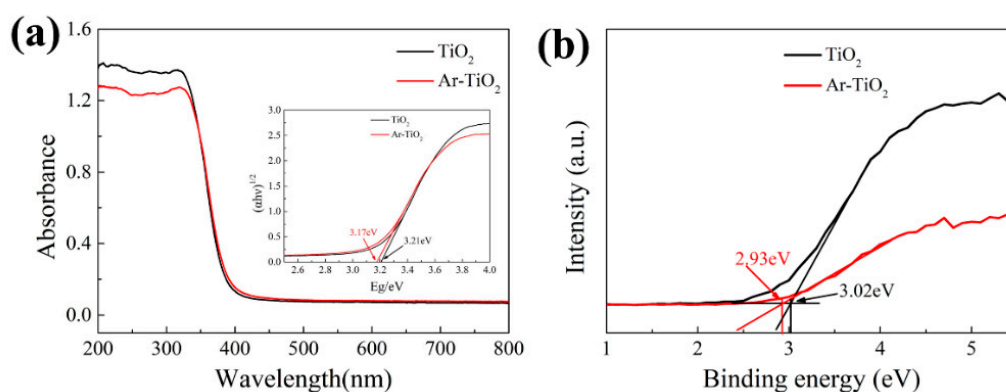
Figure 3. (**a**) Ultraviolet (UV)-visible absorption spectra DRS, the insets in Figure 3 (**a**) is the corresponding plots of transformed Kubelka-Munk function versus the energy of photon, (**b**) XPS valence band spectra.
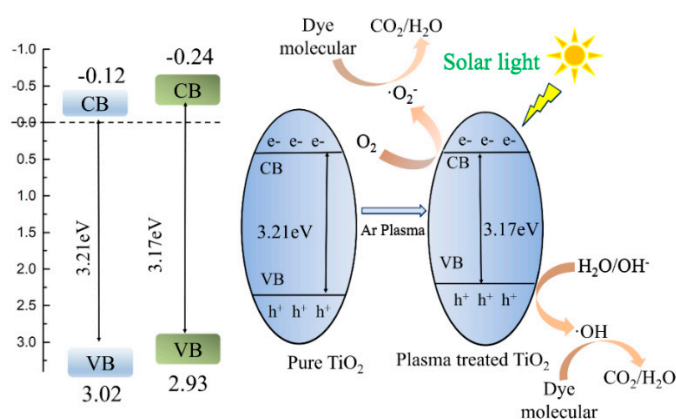
Figure 4. Schematic drawing illustrating the mechanism of charge separation and photocatalytic activity of the TiO_2 photocatalyst under solar light irradiation.

### 3.2. Morphological Characterization

In order to eliminate the impact of catalyst adsorption on photocatalytic performance, BET tests were carried out on the two materials. The N_2 adsorption-desorption isotherms and Barrett-Joyner-Halenda (BJH) pore size distribution curves of TiO_2 and Ar-TiO_2 catalysts are shown in Figure 1d. Both catalyst isotherms are typical type IV isotherms, H1 type hysteresis loops, indicating that the International Union of Pure and Applied Chemistry (IUPAC) classification are a mesoporous material [66]. The BET surface areas of TiO_2 and Ar-TiO_2 were about 124.7 m^2/g and 121.3 m^2/g, respectively (Table 2), indicating that the specific surface areas of the two catalysts were not much different.

Table 2. BET specific surface are, pore volume and pore size of TiO_2 and Ar-TiO_2 catalysts, respectively.

Sample	Surface Area (m^2/g)	Pore Volume (cm^3/g)	Pore Size (nm)
TiO_2	124.7	0.23	5.6
Ar-TiO_2	121.3	0.21	5.6

The pore size distribution (Figure 1d) was determined by the BJH method from the desorption branch of the isotherm, indicating that these TiO_2 nanoparticles have a very pronounced mesoporous structure. The average pore diameters of TiO_2 and Ar-TiO_2 were 5.6 and 5.6 nm, respectively (Table 2). The mesoporous size distribution of the TiO_2 nanoparticles and the mesoporous size distribution of the plasma-treated TiO_2 nanoparticles were not greatly different, indicating that the pore size uniformity of the two materials were near same. The effect of physical adsorption on photocatalytic performance can be ruled out.

TEM and HRTEM images of TiO_2 and Ar-TiO_2 are shown in Figure 5. Figure 5a,d shown that there were no significant changes in the morphology of the TiO_2 after the treatment, and both of them exhibit irregular large spherical nanoparticles. These irregular spherical nanoparticles consist of a plurality of small particles. As shown in Figure 5c, the TiO_2 catalyst showed clear lattice fringes. The lattice spacing values were 0.352, 0.2378 and 0.189 nm, corresponding to the (101), (004) and (200) crystal faces of TiO_2, respectively. However, in Figure 5f, after plasma treatment (Ar-TiO_2), the surface of TiO_2 changed significantly, localized regions were destroyed and uneven, lattice defects were generated, and many deformations occurred. The lattice can increase the amorphous crystal structure and oxygen vacancies [56]. Therefore, defects on the surface of the catalyst after plasma treatment expose more active sites, improving photocatalytic activity.
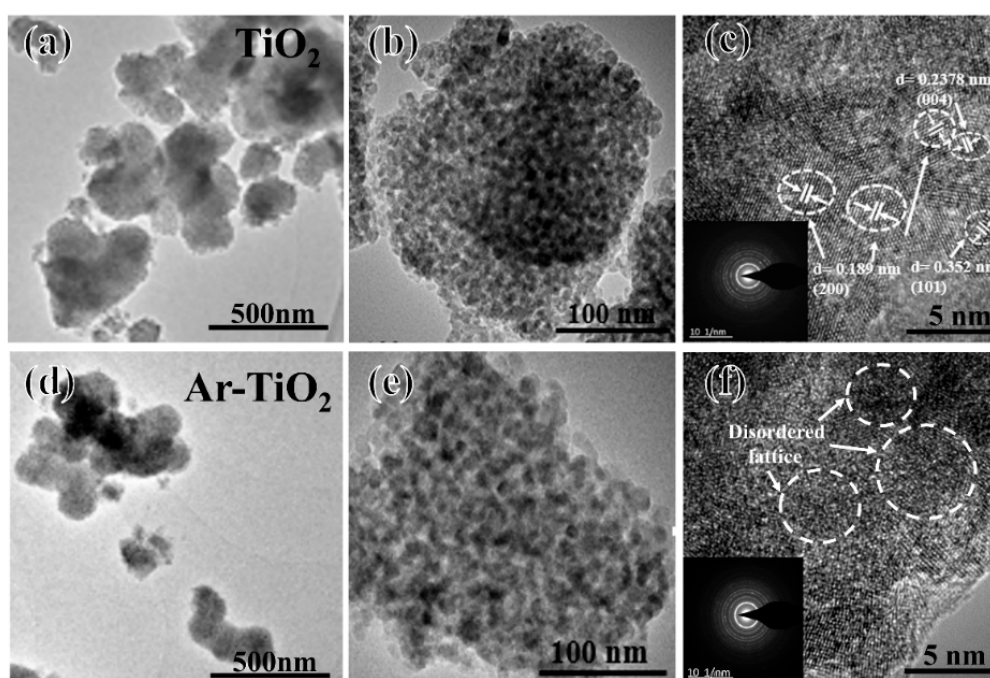
Figure 5. The results of transmission electron microscopy (TEM) of (**a**,**b**) TiO_2 and (**d**,**e**) Ar-TiO_2. High resolution TEM (HRTEM) image curves of (**c**) TiO_2 (inset: SAED) and (**f**) Ar-TiO_2 (insert: SAED).

3.3. Photocatalytic Performance

The photocatalytic degradation experiments of MO, Rho B and MB dye solutions in TiO_2 and Ar-TiO_2 photocatalysts under sunlight and visible light ($\lambda \geq 400$ nm) were estimated. In a typical photocatalytic reaction, TiO_2 absorbs energy greater than its forbidden band width and excites electron-hole pairs in the conduction and valence bands. Then these segregated charges transfer to the catalyst surface to take part in the following photocatalytic degradation reaction. Above all, the strong active O species ($O_2^{-\cdot}$ and $\cdot$OH) produced in the photocatalytic process have superior redox properties and are used to degrade organic pollutants in water, resulting in an effective photocatalytic degradation reaction.

Figure 6a shows that the Ar-TiO_2 (99.6% efficiency) photocatalyst achieved better MO degradation performance than TiO_2 (49% efficiency) after 30 min of sunlight exposure. Degradation rate k ($kt = \ln(C_0/C)$), the degradation rate of the TiO_2 sample was 0.66 h^{-1}, and the degradation rate of Ar-TiO_2 sample was 5.38 h^{-1}. Similarly, Ar-TiO_2 photocatalyst showed excellent performance in the degradation of MO solution after visible light ($\lambda \geq 400$ nm) for 150 min (Figure 6b). The degradation rate of TiO_2 was 0.26 h^{-1}, and the degradation rate of Ar-TiO_2 was 2.14 h^{-1}. As shown in Figure 6c–f, similar results were obtained for additional degradation experiment of Rho B and MB under sunlight and visible light ($\lambda \geq 400$ nm) illumination. The degradation rate after dye degradation is shown in Table 3.
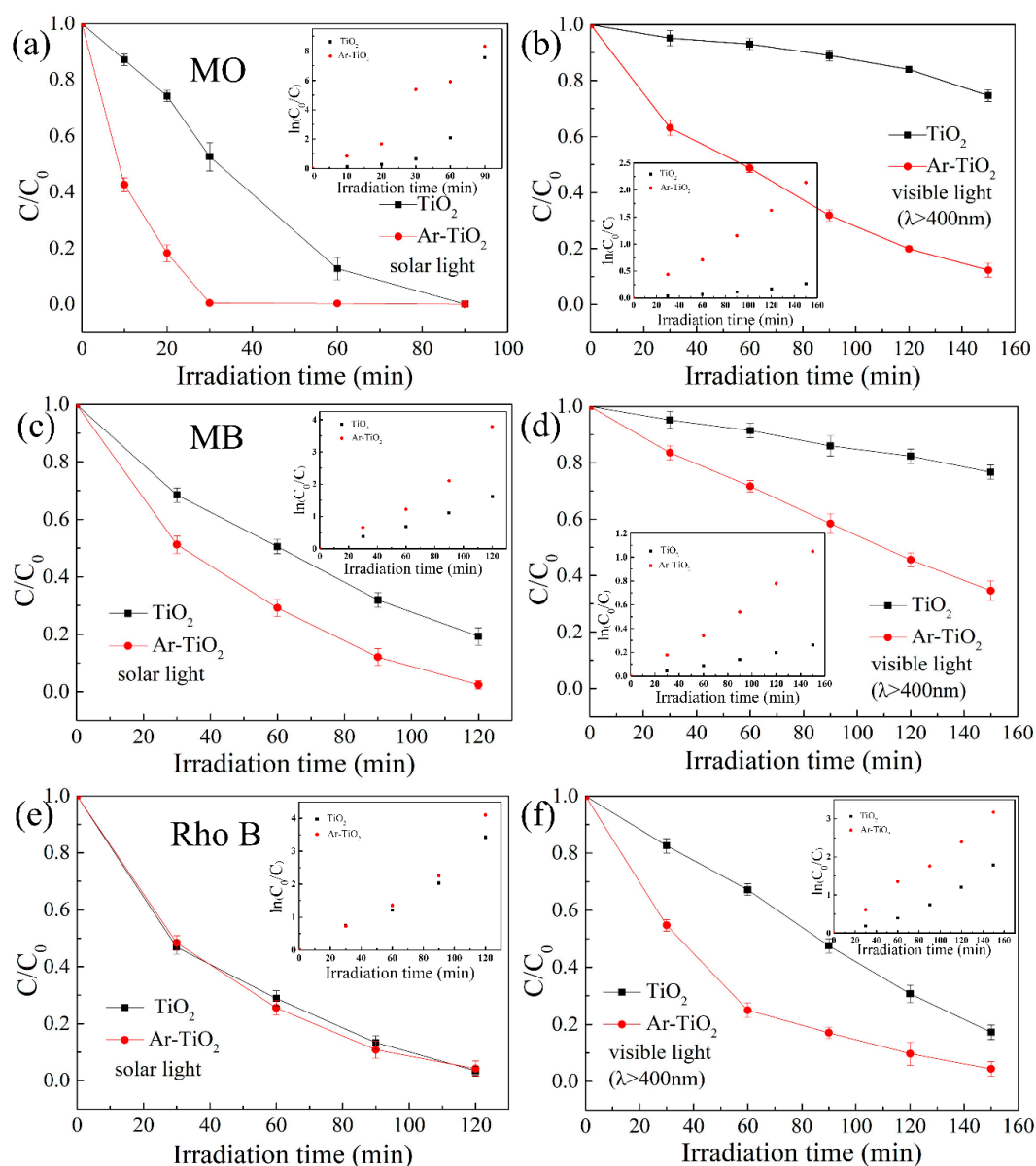
Figure 6. Removal of (**a**,**b**) methyl orange (MO), (**c**,**d**) methylene blue (MB) and (**e**,**f**) rhodamine B (Rho B) by TiO_2 and Ar-TiO_2 (inset: corresponding degradation rate images) under solar light and/or visible light ($\lambda \geq 400$ nm) irradiation. Solution concentration: 10 mg/L; organic solution: 100 mL; catalyst: 50 mg.

Table 3. Degradation rates, k (h^{-1}), of TiO_2 and Ar-TiO_2 after photocatalytic degradation of MO, MB and Rho B dyes.

		TiO_2	**Ar-TiO_2**
MO	solar light	7.55	8.32
	visible light ($\lambda \geq 400$ nm)	0.26	2.14
MB	solar light	1.62	3.78
	visible light ($\lambda \geq 400$ nm)	0.26	1.05
Rho B	solar light	3.42	4.10
	visible light ($\lambda \geq 400$ nm)	1.79	3.17

Figure 6c,e show that the Ar-TiO$_2$ sample has excellent removal performance in the degradation test of Rho B and MB solution under 120 min of sunlight, while the degradation efficiency of the TiO$_2$ sample was relatively lower. Under sunlight, the degradation efficiency of Ar-TiO$_2$ to MO was higher than that of Rho B and MB. Therefore, the photodegradation properties of the Ar-TiO$_2$ sample depend on the dye used, MO (anionic dye), Rho B and MB (cationic dye). This was because the degradation efficiency of the catalyst is impacted by the pH value of the organic dye solution. The pH changed the surface electric charge of TiO$_2$, which affected the adsorption of the organic dye on the surface of TiO$_2$, and influenced the rate on reaction and changed the degradation performance of the photocatalyst [67]. The same test on photocatalyst under visible light ($\lambda \geq 400$ nm) was performed. It can be seen from the Figure 6b,d,f that Ar-TiO$_2$ catalyst exhibited excellent degradation performance in degrading MO, Rho B and MB under 150 min visible light irradiation. The excellent photocatalytic performance of the Ar-TiO$_2$ sample was attributed to the reduction of the TiO$_2$ band gap by plasma treatment, resulting in an expansion of the optical absorption range from the ultraviolet to the visible region, and an increase in the amount of active oxygen and Ti^{3+} defects.

The apparent quantum efficiencies (AQE) of the TiO$_2$ and Ar-TiO$_2$ catalysts was calculated by photocatalytic hydrogen production experiments under full-spectrum conditions. As shown in Table 4, the optical power density was 800 mW·cm^{-2} by the strong optical power meter measured. The number of incident photons were 4.615×10^{19} calculated by the Formula (1) calculated. As can be seen from Table 4, the sample of TiO$_2$ exhibited a H$_2$ evolution rates (HER) of 320 μmol·g^{-1}·h^{-1} with a quantum efficiency of 41.7 % under UV light irradiation ($\lambda = 385$ nm) after 2.5 h. Compared with TiO$_2$, the sample of Ar-TiO$_2$ exhibited the highest H$_2$ evolution rates (530 μmol·g^{-1}·h^{-1}) with a quantum efficiency of 69.0 %. It can be concluded Ar-TiO$_2$ has higher light utilization efficiency.

Table 4. Apparent quantum efficiencies (AQE) and H$_2$ evolution rates (HER) of the TiO$_2$ and Ar-TiO$_2$ catalysts at optical power density of 800 mW·cm^{-2} with incident photon number of 4.615×10^{19}.

Samples	Time (h)	1	1.5	2	2.5
TiO$_2$	HER (μmol·g^{-1}·h^{-1})	98	287	306	320
	AQE (%)	8.7	35.2	39.8	47.7
Ar-TiO$_2$	HER (μmol·g^{-1}·h^{-1})	240	506	524	530
	AQE (%)	31.3	66.0	68.1	69

4. Conclusions

In conclusion, low temperature DBD plasma was successfully employed to treat the surface of TiO$_2$ nanoparticles in Ar atmosphere. The Ar-TiO$_2$ obtained was used for photocatalytic degradation of organic dyes. The results indicated that a large number of oxygen vacancies and Ti^{3+} defects were subsequently generated to promote the decomposition of the reactant molecules, thereby improving the reaction efficiency. Plasma treatment shortened the width of the TiO$_2$ band gap and expanded the light absorption range. The photocatalytic performance indicated that the plasma-treated TiO$_2$ was much better than the original TiO$_2$ nanoparticles in photocatalytic degradation of organic dyes under sunlight. Therefore, plasma can be an effective means to optimize photocatalytic degradation of TiO$_2$ nanoparticles.

Author Contributions: F.Y. conceived, designed and administered the experiments. Y.L. contributed to the synthesis and characterization of materials. W.W., F.W., S.Z. and Y.Y. helped in collected and analyzed data. S.Y. helped to revise the grammar. L.D., B.D. and C.M gave conceptual advice. All authors analyzed, discussed the data and wrote the manuscript.

References

1. Wang, Y.; Zhu, M.; Li, Y.; Zhang, M.; Xue, X.; Shi, Y.; Dai, B.; Guo, X.; Feng, Y. Heteroatom-doped porous carbon from methyl orange dye wastewater for oxygen reduction. *Green Energy Environ.* **2017**, *3*, 172–178. [CrossRef]

2. Song, C.; Zhao, J.; Li, H.; Liu, L.; Xuan, L.; Xing, H.; Liu, H.; Yu, Y. One-pot synthesis and combined use of modified cotton adsorbent and flocculant for purifying dyeing wastewater. *ACS Sustain. Chem. Eng.* **2018**, *6*, 6876–6888. [CrossRef]

3. Vakili, M.; Rafatullah, M.; Salamatinia, B.; Abdullah, A.Z.; Ibrahim, M.H.; Tan, K.B.; Gholami, Z.; Amouzgar, P. Application of chitosan and its derivatives as adsorbents for dye removal from water and wastewater: A review. *Carbohydr. Polym.* **2014**, *113*, 115–130. [CrossRef] [PubMed]

4. Nguyen, N.T.; Altomare, M.; Yoo, J.; Schmuki, P. Efficient photocatalytic H_2 evolution: Controlled dewetting-dealloying to fabricate site-selective high-activity nanoporous au particles on highly ordered TiO_2 nanotube arrays. *Adv. Mater.* **2015**, *27*, 3208–3215. [CrossRef]

5. Nebel, C.E. Photocatalysis: A source of energetic electrons. *Nat. Mater.* **2013**, *12*, 780–781. [CrossRef]

6. Murphy, C.J.; Buriak, J.M. Best Practices for the Reporting of Colloidal Inorganic Nanomaterials. *Chem. Mater.* **2015**, *27*, 4911–4913. [CrossRef]

7. Hoque, M.; Guzman, M. Photocatalytic Activity: Experimental Features to Report in Heterogeneous Photocatalysis. *Materials* **2018**, *11*, 1990. [CrossRef]

8. Boerigter, C.; Campana, R.; Morabito, M.; Linic, S. Evidence and implications of direct charge excitation as the dominant mechanism in plasmon-mediated photocatalysis. *Nat. Commun.* **2016**, *7*, 10545. [CrossRef] [PubMed]

9. Wang, Y.; Sun, H.; Tan, S.; Feng, H.; Cheng, Z.; Zhao, J.; Zhao, A.; Wang, B.; Luo, Y.; Yang, J. Role of point defects on the reactivity of reconstructed anatase titanium dioxide (001) surface. *Nat. Commun.* **2013**, *4*, 2214. [CrossRef]

10. Etacheri, V.; Valentin, C.D.; Schneider, J.; Bahnemann, D.; Pillai, S.C. Visible-light activation of TiO_2 photocatalysts: Advances in theory and experiments. *J. Photochem. Photobiol. C* **2015**, *25*, 1–29. [CrossRef]

11. Pelaez, M.; Nolan, N.T.; Pillai, S.C.; Seery, M.K.; Falaras, P.; Kontos, A.G.; Dunlop, P.S.M.; Hamilton, J.W.J.; Byrne, J.A.; O'Shea, K. A review on the visible light active titanium dioxide photocatalysts for environmental applications. *Appl. Catal. B Environ.* **2012**, *125*, 331–349. [CrossRef]

12. Jenny, S.; Masaya, M.; Masato, T.; Jinlong, Z.; Yu, H.; Masakazu, A.; Bahnemann, D.W. Understanding TiO_2 photocatalysis: Mechanisms and materials. *Chem. Rev.* **2014**, *114*, 9919–9986.

13. Banerjee, S.; Dionysiou, D.D.; Pillai, S.C. Self-cleaning applications of TiO_2 by photo-induced hydrophilicity and photocatalysis. *Appl. Catal. B Environ.* **2015**, *176–177*, 396–428. [CrossRef]

14. Xu, F.; Zhang, J.; Zhu, B.; Yu, J.; Xu, J. $CuInS_2$ sensitized TiO_2 hybrid nanofibers for improved photocatalytic CO_2 reduction. *Appl. Catal. B Environ.* **2018**, *230*, 194–202. [CrossRef]

15. Chen, W.; Wang, Y.; Shangguan, W. Metal (oxide) modified (M= Pd, Ag, Au and Cu) $H_2SrTa_2O_7$ for photocatalytic CO_2 reduction with H_2O: The effect of cocatalysts on promoting activity toward CO and H_2 evolution. *Int. J. Hydrogen Energy* **2019**, *44*, 4123–4132. [CrossRef]

16. Nakata, K.; Fujishima, A. TiO_2 photocatalysis: Design and applications. *J. Photochem. Photobiol. C* **2012**, *13*, 169–189. [CrossRef]

17. Hoffmann, M.R.; Martin, S.T.; Choi, W.; Bahnemann, D.W. Environmental applications of semiconductor photocatalysis. *Chem. Rev.* **1995**, *95*, 69–96. [CrossRef]

18. Fujishima, A.; Zhang, X.; Tryk, D.A. Heterogeneous photocatalysis: From water photolysis to applications in environmental cleanup. *Int. J. Hydrogen Energy* **2007**, *32*, 2664–2672. [CrossRef]

19. Wang, R.; Hashimoto, K.; Fujishima, A.; Chikuni, M.; Kojima, E.; Kitamura, A.; Shimohigoshi, M.; Watanabe, T. Light-induced amphiphilic surfaces. *Nature* **1997**, *388*, 431–432. [CrossRef]

20. Chen, X.; Lei, L.; Huang, F. Cheminform abstract: Black titanium dioxide (TiO_2) nanomaterials. *Chem. Soc. Rev.* **2015**, *46*, 1861–1885. [CrossRef]

21. Xiaobo, C.; Clemens, B. The electronic origin of the visible-light absorption properties of C-, N- and s-doped TiO_2 nanomaterials. *J. Am. Chem. Soc.* **2008**, *130*, 5018–5019.

22. Shin, S.W.; Lee, J.Y.; Ahn, K.S.; Kang, S.H.; Jin, H.K. Visible light absorbing TiO_2 nanotube arrays by sulfur treatment for photoelectrochemical water splitting. *J. Phys. Chem. C* **2015**, *119*, 13375–13383. [CrossRef]

23. Gui-Sheng, L.; Die-Qing, Z.; Yu, J.C. A new visible-light photocatalyst: Cds quantum dots embedded mesoporous TiO$_2$. *Environ. Sci. Technol.* **2009**, *43*, 7079–7085.

24. Jiang, D.; Xu, Y.; Wu, D.; Sun, Y. Visible-light responsive dye-modified TiO$_2$ photocatalyst. *J. Solid State Chem.* **2008**, *181*, 593–602. [CrossRef]

25. Saji, G.; Suman, P.; Zhaoxia, J.; Henderson, B.L.; Tian, X.; Linjiang, L.; Zink, J.I.; Nel, A.E.; Lutz, M.D. Role of fe doping in tuning the band gap of TiO$_2$ for the photo-oxidation-induced cytotoxicity paradigm. *J. Am. Chem. Soc.* **2011**, *133*, 11270–11278.

26. Han, Y.X.; Yang, C.L.; Wang, M.S.; Ma, X.G.; Wang, L.Z. Enhancing the visible-light absorption of TiO$_2$ with the use of key n, co, and na dopant concentrations. *Energy Mater. Sol. Cells* **2015**, *132*, 94–100. [CrossRef]

27. Lee, H.U.; Lee, S.C.; Choi, S.H.; Son, B.; Lee, S.J.; Kim, H.J.; Lee, J. Highly visible-light active nanoporous TiO$_2$ photocatalysts for efficient solar photocatalytic applications. *Appl. Catal. B Environ.* **2013**, *129*, 106–113. [CrossRef]

28. Wan, H.; Yao, W.; Zhu, W.; Yi, T.; Ge, H.; Shi, X.; Tao, D. Fe-N co-doped SiO$_2$ @TiO$_2$ yolk-shell hollow nanospheres with enhanced visible light photocatalytic degradation. *Appl. Surf. Sci.* **2018**, *444*, 355–363. [CrossRef]

29. Chen, S.; Li, X.; Zhou, W.; Zhang, S.; Fang, Y. Carbon-coated Cu-TiO$_2$ nanocomposite with enhanced photostability and photocatalytic activity. *Appl. Surf. Sci.* **2019**, *466*, 254–261. [CrossRef]

30. Aguirre, M.E.; Zhou, R.; Eugene, A.J.; Guzman, M.I.; Grela, M.A. Cu$_2$O/TiO$_2$ heterostructures for CO$_2$ reduction through a direct Z-scheme: Protecting Cu$_2$O from photocorrosion. *Appl. Catal. B Environ.* **2017**, *217*, 485–493. [CrossRef]

31. She, H.; Zhou, H.; Li, L.; Wang, L.; Huang, J.; Wang, Q. Nickel-doped excess oxygen defect titanium dioxide for efficient selective photocatalytic oxidation of benzyl alcohol. *ACS Sustain. Chem. Eng.* **2018**, *6*, 11939–11948. [CrossRef]

32. Hao, C.; Li, J.; Zhang, Z.; Ji, Y.; Zhan, H.; Xiao, F.; Wang, D.; Liu, B.; Su, F.; Hao, C. Enhancement of photocatalytic properties of TiO$_2$ nanoparticles doped with CeO$_2$ and supported on SiO$_2$ for phenol degradation. *Appl. Surf. Sci.* **2015**, *331*, 17–26. [CrossRef]

33. Zha, R.; Nadimicherla, R.; Guo, X. Ultraviolet photocatalytic degradation of methyl orange by nanostructured TiO$_2$/ZnO heterojunctions. *J. Mater. Chem. A* **2015**, *3*, 6565–6574. [CrossRef]

34. Khairy, M.; Zakaria, W. Effect of metal-doping of TiO$_2$ nanoparticles on their photocatalytic activities toward removal of organic dyes. *Egypt. J. Petro.* **2014**, *23*, 419–426. [CrossRef]

35. Choi, H.J.; Kang, M. Hydrogen production from methanol/water decomposition in a liquid photosystem using the anatase structu re of cu loaded. *Int. J. Hydrogen Energy* **2007**, *32*, 3841–3848. [CrossRef]

36. Ganesh, I.; Gupta, A.K.; Kumar, P.P.; Sekhar, P.S.; Radha, K.; Padmanabham, G.; Sundararajan, G. Preparation and characterization of Ni-doped TiO$_2$ materials for photocurrent and photocatalytic applications. *Sci. World J.* **2012**, *2012*, 127326. [CrossRef]

37. Burda, C.; Lou, Y.; Chen, X.; Samia, A.C.S.; Gole, J.L. Enhanced nitrogen doping in TiO$_2$ nanoparticles. *Nano Lett.* **2003**, *3*, 1049–1051. [CrossRef]

38. Jing, L.; Yong, W.; Huang, J.; Jie, F.; Cao, L.; Li, C. In situ synthesis of mesoporous c-doped TiO$_2$ single crystal with oxygen vacancy and its enhanced sunlight photocatalytic properties. *Dyes Pigment.* **2017**, *144*, 203–211.

39. Di, L.; Haneda, H.; Hishita, S.; Ohashi, N. Visible-light-driven N−F−codoped TiO$_2$ photocatalysts. 2. Optical characterization, photocatalysis, and potential application to air purification. *Chem. Mater.* **2005**, *17*, 2596–2602.

40. Ohno, T. Preparation of visible light active s-doped TiO$_2$ photocatalysts and their photocatalytic activities. *Water Sci. Technol.* **2004**, *265*, 115–121. [CrossRef]

41. Sonobe, T.; Yoshida, K.; Hachiya, K.; Bakr, M.A.; Kii, T.; Yoshikawa, S.; Ohgaki, H. Optical studies of the microwave-treated TiO$_2$ photocatalyst by mir-fel. *J. Sustain. Ener. Environ.* **2011**, *2*, 27–29.

42. Pylnev, M.; Chang, W.-H.; Wong, M.-S. Shell of black titania prepared by sputtering TiO$_2$ target in H$_2$ + Ar plasma. *Appl. Surf. Sci.* **2018**, *462*, 285–290. [CrossRef]

43. Bonelli, T.S.; Pereyra, I. Low temperature rf plasma nitriding of self-organized TiO$_2$ nanotubes for effective bandgap reduction. *Appl. Surf. Sci.* **2018**, *442*, 239–244. [CrossRef]

44. Chung, K.H.; Jeong, S.; Kim, B.J.; An, K.H.; Park, Y.K.; Jung, S.C. Enhancement of photocatalytic hydrogen production by liquid phase plasma irradiation on metal-loaded TiO$_2$/carbon nanofiber photocatalysts. *Int. J. Hydrogen Energy* **2018**, *43*, 11422–11429. [CrossRef]

45. Zheng, Z.; Huang, B.; Lu, J.; Wang, Z.; Qin, X.; Zhang, X.; Dai, Y.; Whangbo, M.-H. Hydrogenated titania: Synergy of surface modification and morphology improvement for enhanced photocatalytic activity. *Chem. Commun.* **2012**, *48*, 5733–5735. [CrossRef]

46. Wang, G.; Wang, H.; Ling, Y.; Tang, Y.; Yang, X.; Fitzmorris, R.C.; Wang, C.; Zhang, J.Z.; Li, Y. Hydrogen-treated TiO$_2$ nanowire arrays for photoelectrochemical water splitting. *Nano Lett.* **2011**, *11*, 3026–3033. [CrossRef] [PubMed]

47. Mohammadizadeh, M.R.; Bagheri, M.; Aghabagheri, S.; Abdi, Y. Photocatalytic activity of TiO$_2$ thin films by hydrogen dc plasma. *Appl. Surf. Sci.* **2015**, *350*, 43–49. [CrossRef]

48. Wang, Y.; Yu, F.; Zhu, M.; Ma, C.; Zhao, D.; Wang, C.; Zhou, A.; Dai, B.; Ji, J.; Guo, X. N-Doping of plasma exfoliated graphene oxide via dielectric barrier discharge plasma treatment for the oxygen reduction reaction. *J. Mater. Chem. A* **2018**, *6*, 2011–2017. [CrossRef]

49. Zhao, D.; Yu, F.; Zhou, A.; Ma, C.; Dai, B. High-efficiency removal of NO$_x$ using dielectric barrier discharge nonthermal plasma with water as an outer electrode. *Plasma Sci. Technol.* **2018**, *20*, 014020. [CrossRef]

50. Pan, D.; Han, Z.; Miao, Y.; Zhang, D.; Li, G. Thermally stable TiO$_2$ quantum dots embedded in SiO$_2$ foams: Characterization and photocatalytic H$_2$ evolution activity. *Appl. Catal. B Environ.* **2018**, *229*, 130–138. [CrossRef]

51. Pu, S.; Zhu, R.; Hui, M.; Deng, D.; Pei, X.; Fei, Q.; Wei, C. Facile in-situ design strategy to disperse TiO$_2$ nanoparticles on graphene for the enhanced photocatalytic degradation of Rhodamine 6G. *Appl. Catal. B Environ.* **2017**, *218*, 208–219. [CrossRef]

52. Han, E.; Vijayarangamuthu, K.; Youn, J.S.; Park, Y.K.; Jung, S.C.; Jeon, K.J. Degussa P 25 TiO$_2$ modified with H$_2$O$_2$ under microwave treatment to enhance photocatalytic properties. *Catal. Today* **2017**, *303*, 305–312. [CrossRef]

53. An, H.R.; Yong, C.H.; Kim, H.; Jin, Y.H.; Park, E.C.; Park, S.Y.; Jeong, Y.; Park, J.I.; Kim, J.P.; Lee, Y.C. Studies on mass production and highly solar light photocatalytic properties of gray hydrogenated-TiO$_2$ sphere photocatalysts. *J. Hazard. Mater.* **2018**, *358*, 222–233. [CrossRef]

54. Vinodkumar, E.; Yourey, J.E.; Bartlett, B.M. Chemically bonded TiO$_2$-bronze nanosheet/reduced graphene oxide hybrid for high-power lithium ion batteries. *ACS Nano* **2014**, *8*, 1491–1499.

55. Ullattil, S.G.; Periyat, P. A 'one pot' gel combustion strategy towards Ti^{3+} self-doped 'black' anatase TiO$_{2-x}$ solar photocatalyst. *J. Mater. Chem. A* **2016**, *4*, 5854–5858. [CrossRef]

56. Kong, X.; Xu, Y.; Cui, Z.; Li, Z.; Liang, Y.; Gao, Z.; Zhu, S.; Yang, X. Defect enhances photocatalytic activity of ultrathin TiO$_2$ (B) nanosheets for hydrogen production by plasma engraving method. *Appl. Catal. B Environ.* **2018**, *230*, 11–17. [CrossRef]

57. Pillai, S.C.; Periyat, P.; George, R.; Mccormack, D.E.; Seery, M.K.; Hayden, H.; Colreavy, J.; Corr, D.; Hinder, S.J. Synthesis of high-temperature stable anatase TiO$_2$ photocatalyst. *J. Phys. Chem. C* **2007**, *111*, 1605–1611. [CrossRef]

58. Dzwigaj, S.; Arrouvel, C.; Breysse, M.; Geantet, C.; Inoue, S.; Toulhoat, H.; Raybaud, P. DFT makes the morphologies of anatase-TiO$_2$ nanoparticles visible to ir spectroscopy. *J. Catal.* **2005**, *236*, 245–250. [CrossRef]

59. Kang, I.C.; Zhanga, Q.; Shu, Y.; Satoa, T.; Saitoa, F. Preparation of a visible sensitive carbon doped tio2 photo-catalyst by grinding TiO$_2$ with ethanol and heating treatment. *Appl. Catal. B Environ.* **2008**, *80*, 81–87. [CrossRef]

60. Ou, G.; Xu, Y.; Wen, B.; Lin, R.; Ge, B.; Tang, Y.; Liang, Y.; Yang, C.; Huang, K.; Zu, D. Tuning defects in oxides at room temperature by lithium reduction. *Nat. Commun.* **2018**, *9*, 1302. [CrossRef]

61. Qi, K.; Liu, S.Y.; Qiu, M.; University, N.; University, S. Photocatalytic performance of TiO$_2$ nanocrystals with/without oxygen defects. *Chin. J. Catal.* **2018**, *39*, 867–875. [CrossRef]

62. Hu, M.; Xing, Z.; Yan, C.; Li, Z.; Xu, Y.; Xiu, Z.; Zhao, T.; Yang, S.; Wei, Z. Ti^{3+} self-doped mesoporous black TiO$_2$/SiO$_2$/g-C$_3$N$_4$ sheets heterojunctions as remarkable visible-lightdriven photocatalysts. *Appl. Catal. B Environ.* **2018**, *226*, 499–508. [CrossRef]

63. Xiaobo, C.; Lei, L.; Yu, P.Y.; Mao, S.S. Increasing solar absorption for photocatalysis with black hydrogenated titanium dioxide nanocrystals. *Science* **2011**, *331*, 746–750.

64. Wanbiao, H.; Yun, L.; Withers, R.L.; Frankcombe, T.J.; Lasse, N.; Amanda, S.; Melanie, K.; Paul, S.; Bill, G.; Hua, C. Electron-pinned defect-dipoles for high-performance colossal permittivity materials. *Nat. Mater.* **2013**, *12*, 821–826.

65. Lin, T.; Yang, C.; Wang, Z.; Yin, H.; Lü, X.; Huang, F.; Lin, J.; Xie, X.; Jiang, M. Effective nonmetal incorporation in black titania with enhanced solar energy utilization. *Energy Environ. Sci.* **2014**, *7*, 967. [CrossRef]

66. Yunxia, Z.; Guanghai, L.; Yucheng, W.; Yuanyuan, L.; Lide, Z. The formation of mesoporous TiO_2 spheres via a facile chemical process. *J. Phys. Chem. B* **2005**, *109*, 5478–5481.

67. Kumar, A.; Pandey, G. A review on the factors affecting the photocatalytic degradation of hazardous materials. *Mater. Sci. Eng. Int. J.* **2017**, *1*, 106–114. [CrossRef]